On the measurement of the surface energy budget over a land surface during the summer monsoon

G S Bhat* and S C Arunchandra

Center for Atmospheric and Oceanic Sciences, Indian Institute of Science, Bangalore 560 012, India.
**e-mail: bhat@caos.iisc.ernet.in*

The measurement of surface energy balance over a land surface in an open area in Bangalore is reported. Measurements of all variables needed to calculate the surface energy balance on time scales longer than a week are made. Components of radiative fluxes are measured while sensible and latent heat fluxes are based on the bulk method using measurements made at two levels on a micrometeorological tower of 10 m height. The bulk flux formulation is verified by comparing its fluxes with direct fluxes using sonic anemometer data sampled at 10 Hz. Soil temperature is measured at 4 depths. Data have been continuously collected for over 6 months covering pre-monsoon and monsoon periods during the year 2006. The study first addresses the issue of getting the fluxes accurately. It is shown that water vapour measurements are the most crucial. A bias of 0.25% in relative humidity, which is well above the normal accuracy assumed by the manufacturers but achievable in the field using a combination of laboratory calibration and field intercomparisons, results in about 20 W m^{-2} change in the latent heat flux on the seasonal time scale. When seen on the seasonal time scale, the net longwave radiation is the largest energy loss term at the experimental site. The seasonal variation in the energy sink term is small compared to that in the energy source term.

1. Introduction

Land surface temperature is an important meteorological variable and is required in many practical applications. It is desirable that we understand its evolution on different time scales ranging from few hours (e.g., to predict the occurrence of thunderstorms) to 100s of years (e.g., climate change related issues). The evolution of surface temperature is governed by the surface energy balance. Absorbed solar radiation is the primary source of energy, and long term (i.e., climatic) equilibrium means that this energy is eventually removed from the surface and transferred to the atmosphere. The energy loss can be in the form of sensible (SHF) and latent (LHF) heat fluxes, net long wave radiation (NLW) and advection (Q_A). On shorter time scales, heat flux into the ground (G) and energy storage in the canopies (S) also become important (figure 1).
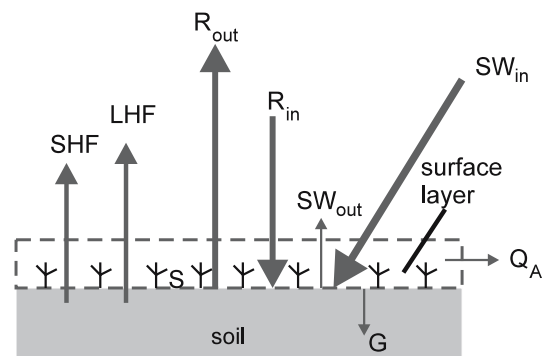

Figure 1. A schematic of the components of energy flux at a land surface. Arrows point the direction of energy transfer and their size is indicative of the relative magnitudes of the components. Surface is assumed to have some vegetation.

In order to understand the surface energy balance on different time scales, we need to know not only

the net surface heat flux (Q_{net}, defined in section 3) but also its individual components. This understanding enters numerical models (e.g., global circulation models and regional models) being run to predict weather and climate.

Among the different components of surface energy balance, radiative fluxes and ground heat fluxes can be measured by the instruments. *SHF* and *LHF* are major loss terms, however, not directly measurable by instruments. So is Q_A but often neglected under the assumption of horizontal homogeneity. In numerical models and for the data coming from routine meteorological observations, *SHF* and *LHF* are estimated from knowing temperature, wind speed and water vapour concentration (or relative humidity, *RH*) and employing empirical relations (so called bulk methods). The Monin–Obukhov (M–O) similarity theory (Monin 1970; Businger *et al* 1971; Monin and Yaglom 1975), which is valid for a convective boundary layer, is the most widely used theory in the estimation of *SHF* and *LHF* (e.g., Kaimal and Finningan 1994). A large number of individual and collective observations have been carried out in the past to understand the atmospheric boundary layer and develop flux relations in forced (e.g., Businger *et al* 1971; Dyer 1974) and natural convection limits (e.g., Rao and Narasimha 2006). These formulations are validated and fine-tuned by comparing their estimated fluxes with those computed from the eddy correlation method (ECM, Businger *et al* 1971; Beljaars and Holtslag 1991). ECM uses the definition of a flux in a stationary turbulent flow due to turbulent fluctuations to estimate *SHF* and *LHF* and hence the fluxes so obtained are also known as direct fluxes. Several assumptions are made in ECM including that the flow is turbulent and stationary (Monin and Yaglom 1975). Experience shows that the conditions in the atmosphere remain stationary less than 20% of the time and that too for durations less than an hour at a time. There are also times when wind speed is low and the boundary layer very stable; the flow may be time dependent but not turbulent in the classical sense. The direct fluxes are normally calculated for the stationary data stretches and used in developing the bulk flux relations. Extensions to non-stationary as well as non-turbulent flow conditions are being attempted (e.g., Mahrt 2007, 2008; Zilitinkevich and Esau 2007), however, these flux algorithms have not been tested sufficiently to apply them routinely.

The main difficulty lies in the fact that there are no direct methods to calculate *SHF* and *LHF* for non-stationary conditions. We know from experience that the heat capacity of the land surface is not large, and therefore on monthly and seasonal time scales, almost all the absorbed solar

energy is returned to the atmosphere. Therefore, one indirect way of verifying the overall accuracy of the surface flux formulations is to look at the long term behaviour of Q_{net}. While a large number of boundary layer experiments have been carried out in the last 50 years, to our knowledge, none of them have addressed the surface energy balance on monthly and seasonal time scales. In the last 10 years, a global network of micrometeorological tower sites are being established under the international FLUXNET programme, where continuous measurements of the exchanges of carbon dioxide (CO_2), water vapor, and energy between terrestrial ecosystem and atmosphere are being carried out (Wilson *et al* 2002). At these sites, radiative fluxes are accurately measured and fluxes of CO_2, water vapor and sensible heat are calculated from ECM using sonic anemometer and infrared sensor data (e.g., Anthoni *et al* 1999; Hollinger *et al* 1999; Schmid *et al* 2000; Wilson and Baldocchi 2000). These FLUXNET sites have been set up in North America, Europe, Australia and Asia (Japan, China, Korea and Thailand) enabling the precise calculations of surface energy balance on different time scales purely based on observed/measured fluxes. Results show that there is a general lack of closure at most sites, with the available energy (net radiation minus the energy stored) larger than the sum of *SHF* and *LHF* (e.g., Wilson *et al* 2002). The mean imbalance is about 20%. (The advection term is neglected in these calculations on the ground that the sites chosen are horizontally homogeneous.)

While such comprehensive measurements are yet to be taken up in India, there have been experiments here where surface fluxes were measured [e.g., the Monsoon Trough Boundary Layer Experiment (MONTBLEX) in 1990 (Narasimha *et al* 1997), Land Surface Processes Experiment (LASPEX) during 1997–98 (Vernekar *et al* 2003)]. One common feature among the previous Indian experiments is that the data time series is discontinuous and continuous measurements covering an entire season are missing. Further, these measurements are not comprehensive in the sense that in some cases radiation data are not available while in other experiments the humidity data. Therefore, continuous time series of sufficient duration and including all variables needed to study the seasonal energy balance based on measured data alone is missing in the Indian context.

The present study, aimed at partially filling this gap, has two main objectives. The first objective is to understand what it takes to experimentally measure the components of the surface fluxes reliably. The second objective is to build a time series that enables the calculation of the seasonal surface energy balance based on the measured fluxes

only. A micrometeorological tower was set up and instrumented at two levels above the ground for this purpose. The experimental arrangement is described in section 2, section 3 briefly explains the theory required to calculate the fluxes, section 4 presents results, discussion is in section 5 and conclusions are in section 6. It is shown that the calculated surface energy balance is very sensitive to even small errors in the relative humidity difference between two levels. The overall required accuracy of temperature and relative humidity measurements is much more than the normal accuracy levels promised by even the best makes of these sensors. A combination of laboratory calibration and intercomparison helps in reducing the inherent differences between the sensors substantially to below the manufacturer specifications. Another finding is that at this location, the net longwave radiation and not *SHF* or *LHF*, is the largest energy loss term during the summer monsoon period.

2. Experimental setup

A 10 m high micrometeorological tower was installed in an open area in the airfield located within the campus of the Indian Institute of Science (IISc), Bangalore, India (13.01°N, 77.34°E). Figure 2 shows a photograph of the tower taken at an angle approximately normal to the then prevailing wind direction. The ground is flat and the tower site is covered with grass and small bushes, and the surrounding area is clear of any tall trees within a radius of at least 50 m. In the upstream direction of wind, natural vegetation (grass) is present over a distance of more than 200 m which is reasonably homogeneous and grass was not cut to maintain the natural conditions even in the immediate neighborhood of the tower. Along the upwind direction, the homogeneity is better than that seen in the photograph and we believe that roughness, albedo and surface emissivity at the tower location are reasonably representative of the upwind area. The fetch (an upwind distance with uniform surface characteristics) along the west and south-west directions (the direction of the prevailing winds during the summer monsoon season) was few hundred meters and along the north and north-east direction (direction of winds during winter) was about 75 m. Table 1 shows the sensor makes and the manufacturer specified accuracies. Temperature (T), relative humidity, horizontal component of wind speed (U) and wind direction instruments were mounted at two levels, namely 2 and 8 m (figure 2). All components of the radiation were measured using radiation instruments (pyranometers and

Figure 2. Photograph showing the experimental setup in the field. Vegetation at the site was allowed to grow naturally.

pyrgeometers) installed on a separate 2 m mast (figure 2). The radiation instruments installed are of Eppley make, regarded to be one of the most reliable, commercially available radiation instruments. Our choice for this make was influenced by its selection in Woods Hole's IMET (Improved Meteorology) system (Hosom *et al* 1995). Soil temperature was measured at 4 depths, namely 0.05, 0.1, 0.15 and 0.2 m. All sensors and data loggers were powered by a 12 V battery which was charged by a solar cell. The data were sampled every 5 seconds, averaged for 2 minutes and stored. Results shown correspond to the period May–October 2006.

Further, a sonic anemometer was installed at 2 m height on the tower and its data were collected during 30 May to 12 July 2006. This sonic anemometer measured three components of wind velocity and air temperature. Data were acquired at 10 Hz rate and stored in a PC. Running the sonic anemometer and PC required much more power than the solar panel could provide. Since the line power was not available at the tower site, these instruments were operated using a car battery, which lasted for about 20 hours when fully charged. Therefore, the sonic anemometer time series is not continuous and there

Table 1. *Sensors used in the present experimental setup and their specifications. These instruments were procured during BOBMEX (Bhat et al 2001) and ARMEX (Bhat et al 2005, Rao 2005), and redeployed after repair or maintenance so that the data accuracies are not compromised.*

Parameter/Instrument	Sensor	Accuracy	Make and model
Air temperature	Platinum resistance thermometer	$\pm 0.2°$C	ROTRONICS, MP100H with Hygroclip S3
Relative humidity	Capacitance	$\pm 1.5\%$	ROTRONIC, MP100H with Hygroclip S3
Pressure	Capacitance	± 0.3 hpa	VAISALA, PTB100A
Wind speed and wind direction	Propeller, potentiometer	± 0.3 m s^{-1} or 1% of reading, $\pm 3°$C	R.M. YOUNG, Wind Monitor 05103
Rain gauge	Tipping bucket	0.1 mm per 50 tips	R.M. YOUNG, 52203
Soil temperature	Platinum resistance thermometer	$\pm 0.3°$C	HONEY WELL, HEL-700, thin film
Multi-plate radiation shield		–	R.M. YOUNG
Shortwave radiation	Thermopile	*absolute accuracy ± 3–4% and relative accuracy $\pm 2\%$	EPPLEY, PSP
Longwave radiation	Thermopile with temperature compensation	* ± 10 W m^{-2}	EPPLEY, PIR
Wind vector (u, v, w)	Sonic anemometer	0.1 m s^{-1}	METEK, USA-1
Temperature	Sonic anemometer	0.01°C	METEK, USA-1
Data logger			Campbell, CR10X

*Eppley does not specify the actual accuracy of their radiation instrument. The numbers are based on the reports from researchers who carried out calibration and intercomparison experiments.

are data gaps. The sonic data are basically used to verify the bulk fluxes, and this purpose was served with the data collected.

The calibration of instruments is very crucial for maintaining the accuracy of measurements. Before installation in the field, temperature and humidity sensors were calibrated in the laboratory. Further, these sensors along with a reference platinum resistance thermometer (Pt1000) were then placed in a closed, insulated chamber having a fan for air circulation, and data collected continuously over one diurnal cycle in the laboratory. This provided data to check the relative differences between similar sensors. The wind sensors (slow sensors) are calibrated using sonic anemometer as the reference by placing all of them at the same height on the tower. The sonic anemometer was independently calibrated earlier in a wind tunnel, and found to perform as per the manufacturer specifications.

3. Theory

Figure 1 shows a schematic of different terms involved in the land surface energy budget. The surface is assumed to have vegetation that forms the interface between the soil surface and the

atmosphere. SW_{in} and SW_{out} are the incoming and reflected fluxes of shortwave radiation, R_{in} and R_{out} are respectively the incoming and outgoing fluxes of longwave radiation. Assuming horizontal homogeneity (Q_A is ignored) and neglecting the energy storage in the interfacial layer (S is neglected), the energy balance at the earth's surface gives,

$$SW_{in} = SHF + LHF + SW_{out}$$
$$+ NLW + G, \tag{1a}$$

$$R_{net} = SW_{in} - SW_{out} - NLW = SHF$$
$$+ LHF + G, \tag{1b}$$

and

$$Q_{net} = SW_{in} - (SW_{out} + NLW$$
$$+ SHF + LHF + G), \tag{1c}$$

where NLW is net longwave radiation ($= R_{out} - R_{in}$). Here, SW_{in} and R_{in} directed towards while

other components directed away from the surface are taken positive. Both equations (1a) and (1b) are identical, however, their interpretations are slightly different. Normally, when such equations are written, uncertainties are thought to be with the *RHS*. In the present case, putting R_{net} on *LHS* gives the impression that radiative fluxes are alright. This is far from the truth. There could be substantial errors in the radiation terms, longwave fluxes, in particular. To emphasize this, we consider equation (1a) along with the more traditional form, namely, equation (1b) which equates the net radiation to the sum of turbulent fluxes (*SHF* and *LHF*) and ground heat flux. Components of radiation can be measured using appropriate radiation instruments. *SHF* and *LHF* are estimated by assuming the flow to be stationary, turbulent and horizontally homogeneous. This leads to the expressions (e.g., Stull 1988):

$$
\left.
\begin{aligned}
SHF &= \rho C_p \overline{w'\theta'} = -\rho C_p u_* \theta_* \\[6pt]
LHF &= \rho L_e \overline{w'q'} = -\rho L_e u_* q_* \\[6pt]
\tau &= -\rho \overline{u'w'} = \rho u_*^2
\end{aligned}
\right\},
\qquad (2)
$$

where τ is the surface shear stress, ρ is air density, u_*, θ_* and q_* are respectively the surface layer scales for horizontal wind speed (U), potential temperature (θ) and specific humidity (q). C_p is specific heat of air at constant pressure, L_e is the latent heat of vaporization, u and w are the horizontal (along the mean wind direction) and vertical components of wind velocity respectively measured with a sensor having frequency response better than 1 Hz. The prime denotes the fluctuating parts of respective variables and the overbar represents time averaging. The terms involving the covariances define the respective fluxes in a turbulent flow. With data from instruments that enable the measurements of turbulent fluctuations in the flow (i.e., fast sensors), covariances can be computed and fluxes obtained. The bulk methods vary in complexity, but nowadays are mostly based on M–O similarity theory for a turbulent convective boundary layer (Dyer 1974; Hicks 1976; Beljaars and Holtslag 1991). The vertical profiles of time averaged quantities are given by (e.g., Panofsky and Dutton 1984):

$$
U = \frac{u_*}{k}\left[\ln\left(\frac{z}{z_{o_m}}\right) - \psi_m(\xi)\right]
$$

$$
\theta - \theta_o = \frac{\theta_*}{k}\left[\ln\left(\frac{z}{z_{os}}\right) - \psi_s(\xi)\right] \qquad (3)
$$

$$
q - q_o = \frac{q_*}{k}\left[\ln\left(\frac{z}{z_{os}}\right) - \psi_s(\xi)\right].
$$

Here, z is height above the surface, z_{om} and z_{os} are surface roughness lengths for velocity and scalar (θ and q), respectively. The subscript o refers to the value of the scalar at the roughness height z_{os}. ψ_m and ψ_s are the M–O similarity functions for U and scalar respectively, and are functions of the stability parameter $\zeta(= z/L$, where L is the Monin–Obukhov length scale). $\zeta < 0, = 0$ and > 0 correspond to unstable, neutral and stable stratification respectively. L is given by (Garratt 1992):

$$
L = \frac{\theta_v u_*^2}{g k \theta_{v*}}. \qquad (4)
$$

θ_v is the virtual potential temperature, and θ_v and θ_{v*} are given by:

$$
\theta_v = \theta(1 + 0.61r), \qquad (5)
$$

$$
\theta_{v*} = 0.61\ \theta q_* + \theta_*(1 + 0.61r),
$$

where r is the mixing ratio and is related to q through the equation $r = q/(1 - q)$. Both r and q are small $[\sim O(10^{-2})]$ and nearly equal. Functions ψ_m and ψ_s are empirically determined. The profile method (PM) is a special case of bulk method when measurements at two or more levels in the surface layer are available. For measurements at 2 levels, equations (3) can be rearranged to give:

$$
U_2 - U_1 = \Delta U = \frac{u_*}{k}\left[\ln\left(\frac{z_2}{z_1}\right) - \psi_m(\xi_2) + \psi_m(\xi_1)\right]
$$

$$
\theta_2 - \theta_1 = \Delta\theta = \frac{\theta_*}{k}\left[\ln\left(\frac{z_2}{z_1}\right) - \psi_s(\xi_2) + \psi_s(\xi_1)\right]
$$

$$
q_2 - q_1 = \Delta q = \frac{q_*}{k}\left[\ln\left(\frac{z_2}{z_1}\right) - \psi_s(\xi_2) + \psi_s(\xi_1)\right]
$$

$$
(6)
$$

where, $\xi_1 = z_1/L$ and $\xi_2 = z_2/L$, and the subscripts 1 and 2 refer to lower and upper measurement levels respectively. If wind, temperature and

humidity data are available at 2 levels, then, equations (4)–(6) can be solved (iteratively) to obtain u_*, θ_* and q_* which when used with equation (2) give *SHF* and *LHF*. Note that this method does not assume a drag (or exchange) coefficient. The M–O similarity functions used in this work are based on the works of (Dyer 1974; Beljaars and Holtslag 1991) and are given in Appendix 1.

3.1 *Eddy Correlation Method (ECM)*

The terms involving the covariances in equation (2) define the respective fluxes in a turbulent flow, and the method of calculating fluxes through computing covariances is known as ECM. With sonic anemometer data sampled at 10 Hz, it is possible to compute the covariances and calculate fluxes. Implicit assumption in ECM is that the flow is stationary which is not the case in the atmosphere a majority of the time. The fluxes calculated using ECM are reliable if the flow remains stationary over a time interval of at least 15–30 minutes, and the fluctuating quantities are based on the averages taken over this time interval. Strict stationarity is rarely satisfied in the atmosphere. Statistical tests can be applied to determine if the flow is stationary. This is usually done by dividing the averaging time into two equal parts and calculating the mean and the standard deviation for the two intervals. Then student's t and F tests are applied to the means and standard deviations respectively to determine if the time series satisfies stationarity (e.g., Bendat and Piersol 1986). For the averaging time of 20 minutes used in this study and for the flow conditions that prevailed during a majority time of the observations, 95% confidence limit was satisfied if the means and standard deviations in the two intervals were within 5% of each other. Therefore, we used the simple criteria that if both the mean and standard deviations are within 5% of each other when calculated for each half of the averaging time interval separately, then the flow is stationary.

In the application of ECM, sensor alignment is very critical (Wilczak *et al* 2001). Ideally, the tower site should be on level ground and homogeneous, and the vertical axis of the sonic anemometer parallel to normal to the surface. In this perfectly aligned system, the vertical component of velocity averaged over about half an hour is close to zero. Perfect alignment is very difficult to achieve in the field. If the vertical axis is tilted, then the measured vertical velocity includes a component of the horizontal velocity which causes significant errors in the fluxes computed by ECM. The alignment can be checked by plotting the mean vertical velocity against the mean horizontal wind speed
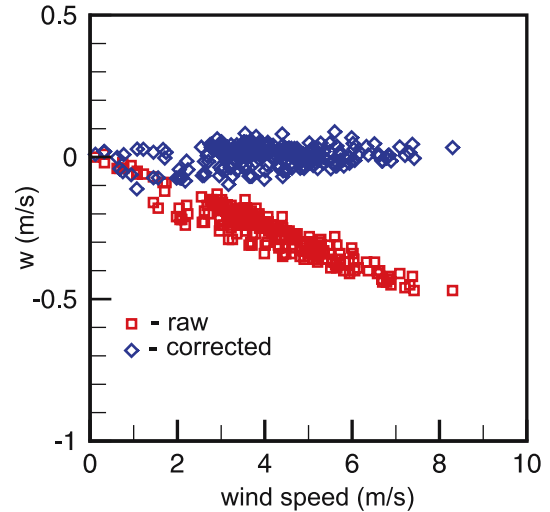

Figure 3. Variation of the 30-minute average vertical velocity (w) with the horizontal wind speed, both measured by the sonic anemometer. Raw and corrected refer to uncorrected and corrected vertical velocity.

(figure 3). Any systematic trend implies that the vertical alignment is not perfect, and this is the case in figure 3 implying that the measured vertical velocity was not normal to the mean streamlines. The vertical inclination works out to be 3.6° at an azimuthal angle of 258° from north. This could have resulted from ground slope or sensor inclination. If this was due to terrain, then, the terrain height should have changed by 1 m for every 16 m horizontal distance. Visual inspection of the ground shows that the ground slope is much less than this. Hence, we primarily attribute the cause to sensor inclination. By a co-ordinate rotation, the true vertical velocity can be obtained. The wind vector was corrected accordingly (figure 3) before calculating the fluxes by ECM. The difference between the fluxes computed from ECM with and without correction for the vertical tilt is found to be about 20% with uncorrected values being larger.

4. Results

4.1 *Mean conditions*

The time series of daily average T, q, U, soil temperature and rainfall are shown in figure 4. Seasonal trends as well as fluctuations on synoptic (i.e., few days) to monthly (i.e., intra-seasonal) time scales are observed. The mid and later half of May had few showers and the daily rainfall exceeded 20 mm on a couple of occasions. Between mid May and June beginning, air and soil temperatures decreased by 5–7°C and q increased by about 4 g kg^{-1}. It is observed from figure 4 that the
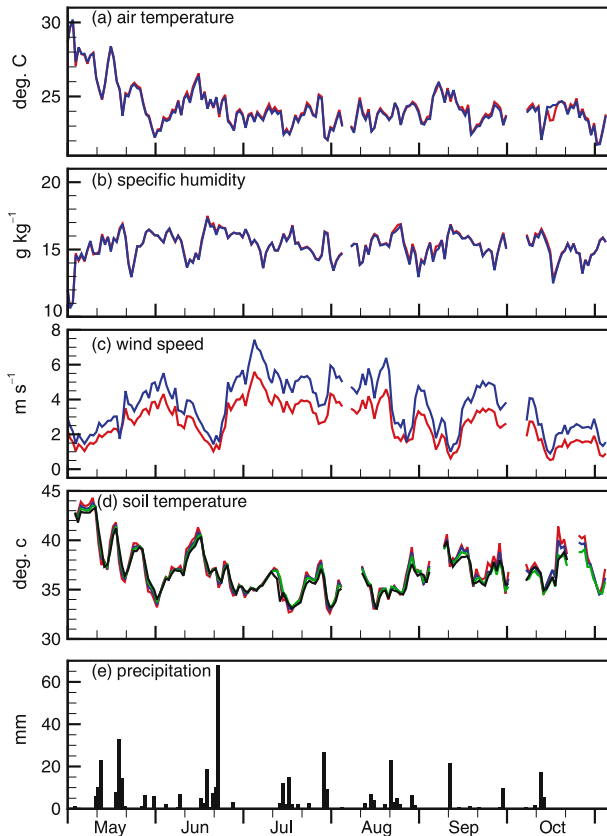
Figure 4. Temporal variation of the daily average values of (**a**) air temperature, (**b**) specific humidity, (**c**) wind speed, (**d**) soil temperature at 0.05, 0.1, 0.15 and 0.2 m depths, and (**e**) precipitation.

differences in temperatures and specific humidities between 2 and 8 m heights are very small on most days [note that these small differences matter in flux calculations, see equation (6)], whereas, that in wind speed is clearly discernible. Wind speeds are higher during the summer monsoon period. The wind speed at 2 m height remained below $5 \, \text{m s}^{-1}$ throughout the observation period while that at 8 m height is larger and the maximum value exceeded $7 \, \text{m s}^{-1}$. Soil temperature between 0.05 and 0.2 m is nearly uniform for a majority of the time. On monthly and seasonal time scales, the change in soil temperature is small. This provides a constraint to the surface energy budget (discussed later). The peak monsoon season in Bangalore is during August–October. The number of rainy days was several during this period (figure 4e), however, most of the rain events were weak and only on three occasions rainfall around $20 \, \text{mm day}^{-1}$ occurred. Fraction of the total time when it actually rained is only 1.1%. The annual rainfall measured in the IISc campus in the year 2006 was 632 mm, very low when compared to that of 2004 (1081 mm) and 2005 (1442 mm). Thus, the study year was relatively dry.

4.2 *Further refining variables and fluxes*

With the measurements available at 2 levels, *SHF* and *LHF* are calculated using equations (4)–(6). The initial values did not appear alright. For example, calculated *LHF* was as large as $-100 \, \text{W m}^{-2}$ during some nights but the atmosphere was dry. Similarly, *SHF* exceeded $-100 \, \text{W m}^{-2}$ during nights and day time values exceeded $600 \, \text{W m}^{-2}$. To check if sensors retained the initial calibration or not, temperature and humidity sensors were brought back to the laboratory and calibrated again. There was no degradation in the performance of the sensors. With calibration, the uncertainty in the temperature of each sensor can be reduced to 0.1°C and that in *RH* to around 1%. These values are smaller than the usual manufacturer specified accuracy levels (which are typically not better than 0.2°C and 1.5% for *T* and *RH* respectively, table 1). In the profile method, calculated fluxes are very sensitive to even small systematic biases between the sensors. Calculations show that even after careful calibration, uncertainties in *SHF* and *LHF* remain high (20% or larger). To further reduce the inherent instrument differences, wind, temperature and humidity sensors were mounted at the same height (8 m) and data collected continuously for few days. There were small but systematic differences between the two sensors measuring the same variable. The constants of the sensors at 2 m height were fine tuned to match the values measured by the sensor mounted at 8 m level for the intercomparison period. Further, it was observed that the response of the humidity sensor at 2 m height is non-linear above 86% *RH* (figure 5a), and a look-up table was prepared for $RH > 86\%$ to convert measured voltage into *RH* for this sensor. After the corrections, the rms values of $\Delta RH (= RH_2 - RH_1)$ and $\Delta T (= T_2 - T_1)$ are 0.23% and 0.04°C respectively (figure 5c–d). Thus, with the help of laboratory calibration and intercomparison exercises, the systematic differences between respective sensors were brought down to levels well below the manufacturer specified accuracies.

Despite all these efforts, values of *SHF* exceeded $-100 \, \text{W m}^{-2}$ on some occasions (figure 6a). These cases were examined in detail to understand the reasons for the large and negative values of *SHF*. A representative time series of *SHF*, ΔT and *u* for such cases are shown in figure 6. Often, the low values of *SHF* occurred under calm conditions during night time. Air was more or less still at 2 m height and about 0.5 to $1 \, \text{m s}^{-1}$ at 8 m height, and ΔT values were as large as $-2°$ to $-3°$C (figure 6c). This resulted in large negative values in *SHF* since only the difference between the wind speeds at 2 levels appears in equation (6) and not the magnitudes
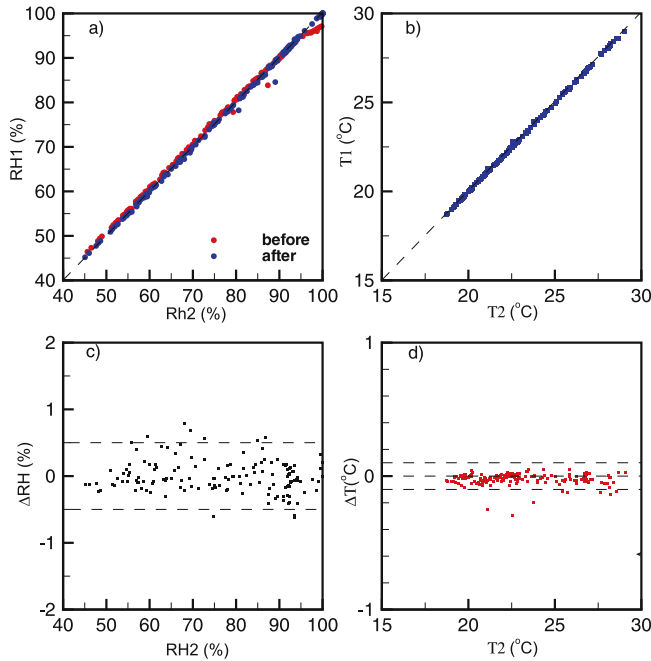
Figure 5. Comparison of relative humidity and air temperature measured by the respective sensors during the intercomparison period. Data are 20-minute averages. 1 and 2 refer to measurement levels. **(a)** relative humidity, **(b)** air temperature, **(c)** ΔRH *vs. RH*, and **(d)** ΔT *vs. T*. In panel a), before and after refer to *RH* measured by the sensor installed at 2 m height before and after the corrections.

Figure 6. **(a)** Temporal variation of *SHF* during the study period. Panels **(b)**–**(d)** show the variation of *SHF*, ΔT and wind speed during 7–12 October 2006. Note that wind speed at level 2 is larger.

of the wind speeds. The implicit assumption in deriving equation (6) is that the boundary layer is turbulent and convective. This assumption breaks down during calm clear nights.

Therefore, it became clear that the problem arises during the night time under low wind conditions where still atmosphere is occasionally interrupted by (mild) wind bursts (Nakamura and Mahrt 2005). For this case, M–O similarity theory is not applicable and the estimation of *LHF* and *SHF* under such conditions remains a major challenge as stated in the introduction. The problem is not trivial because there is no independent method of measuring *SHF* and *LHF* in the field other than through the measurements of wind speed, temperature and water vapour, and under the assumption that the flow is stationary. For the present purpose, hoping that comparing fluxes from two different methods may provide some hints, we compared the PM based fluxes with those based on ECM. One important fact to be noted in this comparison is that sonic anemometer measures the virtual temperature T_v (temperature that accounts for the effect of water vapour on air density) and not the actual air temperature T. T_v is given by (Garratt 1992, p 22).
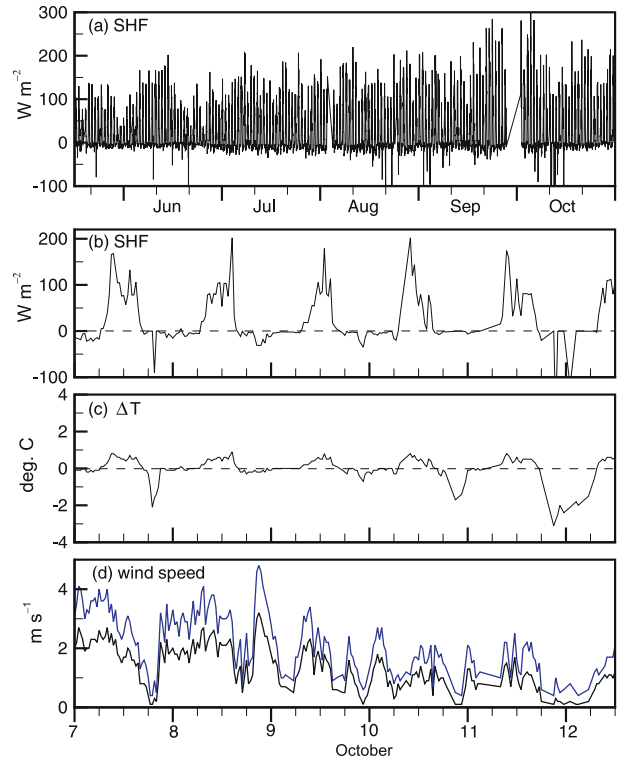
$$T_v = (T + 273.16)(1 + 0.608^* r) - 273.16. \qquad (7)$$

Here T_v is in degree Celsius. Therefore the correlation $\rho C_p \overline{w'\theta'_s}$ [where θ_s is the potential temperature based on sonic temperature T_v, see equations (2) and (5)] is not conventional *SHF*. For the convenience of reference, henceforth it is denoted by SHF_v. The corresponding flux calculated using PM is given by $SHF_v = \rho C_p u_* \theta_{v*}$ [where θ_{v*} is defined in equation (5)]. The values of SHF_v were calculated for an averaging time of 1200 s. For the entire sonic anemometer time series data collected during June–July 2006 (with data gaps), only 422 data stretches satisfied the stationarity conditions. Among these, wind speed below 1 m s^{-1} occured in only one case. In order to increase the number of data points below 2 m s^{-1}, sonic data time series was high band pass filtered to remove slowly varying components having time periods of more than 5 minutes (the reason being, major contribution to turbulent flux comes from frequencies higher than that corresponding to 5-minute periods, e.g., Nakamura and Mahrt 2005). The fluxes are calculated for the filtered data for each 20-minute interval. For the same averaging time interval, SHF_v is calculated using PM.

The outcome of this exercise is shown in figure 7. This figure also shows a comparison of the wind speeds measured at 2 m height by sonic and
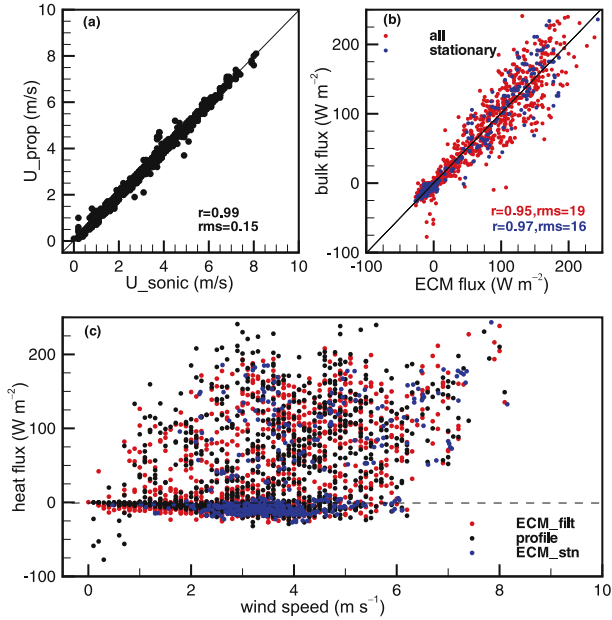
Figure 7. **(a)** Comparison of wind speeds measured by sonic and propeller anemometers at 2 m height. **(b)** Comparison of SHF_v from ECM and PM. **(c)** Variation of SHF_v with wind speed at 2 m height. Correlation coefficient (r) and rms errors (in respective units) are shown in panels (a) and (b). ECM_filt and ECM_stn refer to ECM fluxes for filtered and stationary time series.

propeller anemometers. In figure 7(b), SHF_v calculated from PM is plotted against those calculated from ECM for stationary and filtered time series. There is no noticeable bias or trend between the fluxes from the two methods for both the time series for positive values of SHF_v. However, a major difference is observed at negative values of SHF_v. This occurs in the low wind regime (figure 7c). SHF_v from ECM calculated for stationary time series did not go below $-10\,\mathrm{W\,m^{-2}}$ at wind speeds less than $2\,\mathrm{m\,s^{-1}}$ during night times. However, the number of data points in this wind speed range is too few to draw statistically significant conclusions. The number of data points are more for fluxes based on filtered time series, and if negative values of SHF_v are only considered, the average value of SHF_v is $-12\,\mathrm{W\,m^{-2}}$ for wind speed around $2\,\mathrm{m\,s^{-1}}$ and approach zero for wind speeds below $0.1\,\mathrm{m\,s^{-1}}$. On the other hand, SHF_v based on the bulk method shows some large negative values for wind speeds below $1\,\mathrm{m\,s^{-1}}$. As explained earlier, M–O similarity theory is not applicable for these cases. Therefore, if the wind speed at 2 m level is less than $2\,\mathrm{m\,s^{-1}}$ and SHF_v goes below $-12\,\mathrm{W\,m^{-2}}$, then it seems reasonable to replace this by a value between $-12\,\mathrm{W\,m^{-2}}$ and zero depending on the wind speed (by a linear regression).

Finally, what we need is SHF and not SHF_v for heat budget calculations. Comparing SHF and

SHF_v (both by PM) showed that the two differ from each other by less than a $\mathrm{W\,m^{-2}}$ if the absolute value of SHF_v is less than $50\,\mathrm{W\,m^{-2}}$. Therefore, we extend the results obtained for SHF_v to SHF if the wind speed at 2 m level is below $2\,\mathrm{m\,s^{-1}}$ and the flux is negative. Same criterion is applied to LHF as well.

4.3 *Surface energy balance*

In order to understand the relative importance of different components involved in the surface energy balance, we present the energy source and sink terms separately. In the following, SW_{in} is taken as the energy source and the terms on the right hand side in equation (1a) together are taken as the energy sink. Traditionally, equation (1b) is used to look at the surface energy imbalance. For reasons stated in section 3, we show results for both equations in the following. Thus, the cumulative average source and sink are (ignoring the contribution of ground heat flux G),

$$
\left.\begin{array}{l}
\mathrm{Source} = \dfrac{1}{n}\sum_{i=1}^{n}(SW_{\mathrm{in}})_i \\[2ex]
\mathrm{Sink} = \dfrac{1}{n}\sum_{i=1}^{n}(SHF + LHF \\[1ex]
\qquad\qquad + NLW + SW_{\mathrm{out}})_i
\end{array}\right\}, \qquad (8a)
$$

$$
\left.\begin{array}{l}
R_{\mathrm{net}} = \dfrac{1}{n}\sum_{i=1}^{n}(SW_{\mathrm{in}} - NLW - SW_{\mathrm{out}})_i \\[2ex]
TF = \dfrac{1}{n}\sum_{i=1}^{n}(SHF + LHF)_i
\end{array}\right\}, \qquad (8b)
$$

where i refers to time. For calculating the source and sink in equation (8), LHF and SHF are estimated taking 30-minute averaged values and radiative fluxes are also averaged over the same time interval (giving 48 values per day). The resulting fluxes are added up and the average is taken. Since SW_{in} has strong diurnal dependence, missing data can lead to biases in the cumulative average. Therefore, only those days with complete 24-hour data are considered while calculating the summations in equation (8). The integration started from May 15. Owing to strong diurnal variation in SW_{in}, source shows large amplitude fluctuations initially and it takes few days before its diurnal fluctuations subside. Figure 8(a) shows the temporal variation of individual terms in the sink, and source and sink are compared in figure 8(b) and figure 8(c) shows R_{net} and TF.

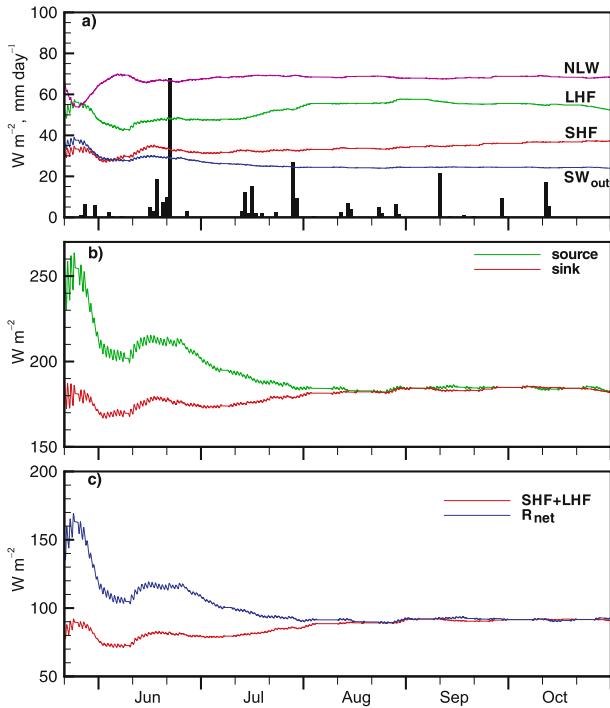During the May–October period, the largest among the sink terms is NLW with an average value

Figure 8. **(a)** Temporal variation of components of energy equation. Also shown in the same panel is daily rainfall. **(b)** Variation of source and sink. **(c)** R_{net} and TF. Note that the values shown here are cumulative average values.

Figure 9. **(a)** The variation of monthly average net radiation and turbulent fluxes during May–October. May average is based on observations made during 15–31 May. **(b)** Monthly variation of the closure ratio. The dashed line indicates a CR value of unity where energy gained through net radiation is lost through turbulent fluxes.

sink terms during this period (figure 8a). The average soil temperature decreased from around 41°C to 34°C during this period (figure 4), and thus ground also lost heat. During June also imbalance remained but reduced to around 25 W m^{-2}. The differences between source and sink are about 26% and 10–12% of the source term during May and June respectively. Soil temperature did increase during the first half of June, but the increase was arrested after the second week and temperature started falling and the net change during the month is small (figure 4d). In equation (1), the contribution from precipitation has been neglected. Since the amount of precipitation has been measured, it is possible to estimate the contribution from it. Calculations show that the contribution from rainfall is not more than a few W m^{-2}. Therefore, the energy imbalance during May–June cannot be attributed to ground heat flux and precipitation. Whether advection was so large or not, cannot be answered from the present experimental arrangement.

Figure 9 shows the monthly variation of TF and R_{net} and the closure ratio $CR(= TF/R_{\text{net}})$. TF is minimum during May, increases subsequently and peaks during August. R_{net} is maximum during May and minimum during July. CR value of more than unity means that more energy is lost due to turbulent fluxes than received through net radiation.

5. Discussion and conclusion

The present study covers the period second half of May to October end. It would have been nice to study the surface energy balance during the transition from winter to summer months too where LHF is expected to be small. In fact, the tower installation started in November 2005; however, it took six months to get all measurements in order to obtain continuous data. The present set of measurements and analysis have given ideas about the problems to be overcome, both instrument and

of 68 W m^{-2}, followed by LHF with an average value of 52 W m^{-2}, SHF is third at 37 W m^{-2} and the smallest term is SW_{out} at 24 W m^{-2}. Owing to (intermittent) rains, soil had moisture and a substantial part of the energy came out in the form of water vapour. This could be a feature over the land surface during the monsoon. We were expecting SHF to be the dominant component over the land surface, but this is not the case. The sum of the two radiative components (92 W m^{-2}) and sum of SHF and LHF (89 W m^{-2}) are nearly equal (the difference is within experimental error), i.e., the energy loss through radiative processes is as large as that due to the turbulent fluxes (TF).

Both figures 8(b) and 8(c) show similar trends and differences are mainly in the magnitudes. Therefore, we discuss figure 8(b) here and the same applies to figure 8(c) as well. The sink is more or less steady and its seasonal variation is relatively small (168 to 188 W m^{-2} and settles around 180 W m^{-2} from August onwards), whereas the source is around 250 W m^{-2} during late May, and gradually decreases to around 180 W m^{-2} as the monsoon season progressed. If we consider the period May–July, source is larger than sink (figure 8b). Before the monsoon onset, there is a large gap between source and sink and during the second half of May the average difference between them is 65 W m^{-2}, i.e., larger than the individual
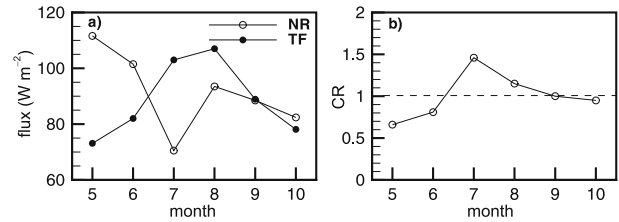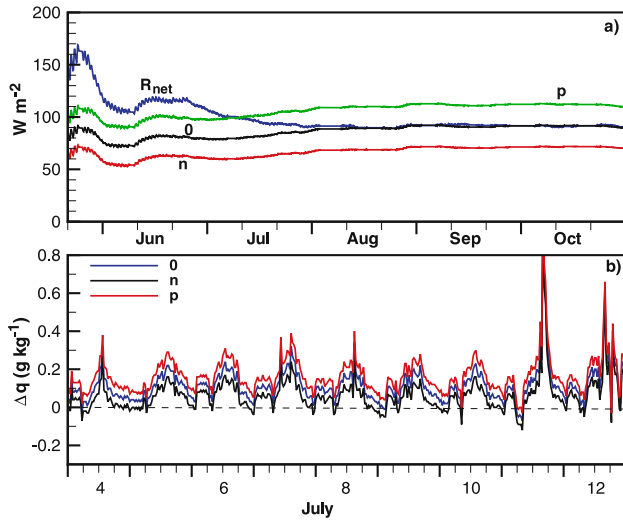
Figure 10. **(a)** Sensitivity of TF to variation in ΔRH. **(b)** The temporal variation of Δq. 0, n and p refer to 0, -0.25%, and $+0.25\%$ perturbations to ΔRH.
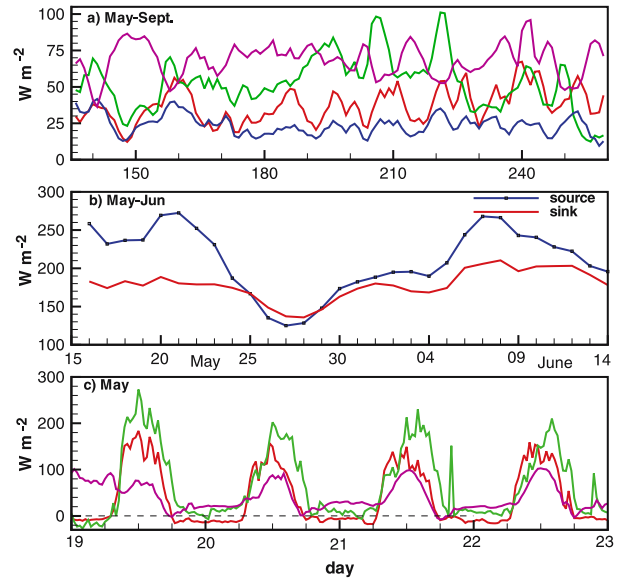

Figure 11. Components of surface heat flux. **(a)** SHF (red), LHF (green), NLW (pink) and $SW_{\rm out}$ (blue) for May–October period. Days with missing data have been removed and x-axis initially represents the Julian day but after day 180, successive days with data. **(b)** Source and sink terms. **(c)** SHF (red), LHF (green) and NLW (pink) during 19–22 May. Fluxes in (a) and (b) are 3-day running average values whereas in (c) is 30-minute average.

theory related, when attempting surface energy balance on seasonal time scales using slow sensor data. The stably stratified low wind cases are frequent over land and ways to obtain fluxes during such conditions need to be devised and standardized. One important result from the present study is the large contribution of the net longwave radiation to surface energy budget. In the Indian field programmes, measurement of longwave radiation has not been given high priority so far, and going by the present results, it is important that both shortwave and longwave radiation are measured accurately. This point needs emphasis because there are several programmes in the country where detailed boundary layer measurements are being planned using instrumented towers. This includes the STORM (Severe Thunderstorms – Observations and Regional Modeling) in the northeastern India, PROWNOM (Prediction of Regional Weather with Observational Meso-Network and Atmospheric Modeling) in south India and CTCZ (Continental Tropical Convergence Zone) in north India. If these efforts are to yield scientifically valuable results, then issues related to the selection of sensors, measurement accuracy, calibration and on site intercomparison, are to be adequately addressed. It is hoped that the present study provides useful information to those planning to make tower measurements with instruments at multi-levels.

It is important to understand how sensitive the energy closure is to errors/uncertainties in ΔT and ΔRH. It is noted in the previous section that the rms values of ΔRH and ΔT are 0.23% and $0.04°C$ respectively. We changed ΔRH and ΔT by $\pm0.25\%$ and $\pm0.05°C$ respectively (i.e., comparable

to respective rms difference) and examined the changes in SHF and LHF (radiative components remain the same). There is little change in SHF and LHF for the specified change in ΔT. However, when ΔRH is perturbed by $\pm0.25\%$, the change in LHF is about $20\,{\rm W\ m}^{-2}$ (figure 10a), i.e., comparable to the contribution of $SW_{\rm out}$ (figure 8a). The reason for the large impact of RH is that the magnitude of Δq is less than $0.3\,{\rm g\ kg}^{-1}$ a majority of the time (figure 10b) and the perturbations caused in Δq due to the above changes in ΔRH are about $\pm0.06\,{\rm g\ kg}^{-1}$, which is a significant fraction of Δq.

One question that naturally arises after an examination of figure 8 is, why the budget does not close during the pre-monsoon period but does so during August–October months? Is it because the terms neglected were important during the pre-monsoon period, or calibration drifted, or due to errors in measurement or in flux algorithms? We don't have a satisfactory answer to all these questions, however, there is no harm in looking at the components of the fluxes during the period when the difference between source and sink are the largest. This happened during 15–23 May with the difference peaking ($\sim 90\,{\rm W\ m}^{-2}$) on 20–21 May (figure 11). Soil temperature increased at a rate of little over a degree Celsius per day during 20–22 May (figure 4). The corresponding estimated ground heat flux is about $30\,{\rm W\ m}^{-2}$ [assuming that

the top 1.5 m layer of the soil is uniformly heated, a soil density of 1500 kg m^{-3} (measured) and soil specific heat of 1200 J kg^{-1} K^{-1} (Farouki 1986)]. This roughly accounts for one third of the difference between source and sink.

The daily average value of SW_{in} is the highest during 20–22 May (~ 270 W m^{-2}, figure 11b) compared to any other day during the entire study period. Theoretically calculated daily average solar insolation at the top of the atmosphere is more than 440 W m^{-2} for the month of May for Bangalore latitude. Therefore, there is no reason to doubt SW_{in} data for these days which were generally cloud free. The diurnal variations in SHF, LHF and NLW are shown in figure 11(c). The lowest value of NLW during May–October period occurred around 20 May (figure 11a). On these days, values of NLW just after the sunset reduced to zero, whereas, during say, August or September, the lowest value of NLW is about 30 W m^{-2} (figure not shown). It is not clear why NLW was so low around 20 May. Further, both LHF and SHF are either very small or negative at night time. The wind speed (at 2 m height) was in 2–4 m s^{-1} range even during the night time; therefore these were not calm nights to produce a very stable surface layer. A careful analysis of data under similar synoptic conditions is needed to check if the negative turbulent fluxes are real or due to sensor drift. As pointed out earlier in this section, drifts in the humidity sensor is very critical to LHF estimation and even a small change of 0.25% in ΔRH can lead to 20 W m^{-2} change in LHF. It may be noted that detailed inter-comparison was carried out towards the end of September. However, now there is no way of knowing the extent of drift between May and September, if there was any. One way to overcome such problems in future is to carry out the intercomparison exercises more frequently and have more than one set of sensors at each level (to avoid data loss during intercomparisons). Further studies with regular intercomparisons and covering an entire year will provide insights into the missing elements in the surface energy balance.

To summarize, this is the first experiment carried out in India that addressed the surface energy balance on a seasonal time scale. It is shown that with a combination of laboratory calibration and field intercomparisons, measurement accuracies in temperature and relative humidity can be substantially improved over the manufacturer specifications. Important findings are as follows:

- When seen on the seasonal time scale, the net longwave radiation is the largest energy loss term at the experimental site.

- A bias of 0.25% in the relative humidity difference between the two levels results in about 20 W m^{-2} change in the latent heat flux. To achieve this level of accuracy, laboratory calibration and field intercomparison are required.

- The seasonal variation in the energy sink term is small compared to that in the energy source term.

Appendix 1

The following similarity functions are used in the calculation of fluxes.

Unstable case: Dyer (1974):

$$\psi_m = 2\ln\left[\frac{(1+x)}{2}\right] + \left[\frac{(1+x^2)}{2}\right] - 2\tan^{-1}(x)$$

$$+ \frac{\pi}{2} \quad \{-0.01 > \xi > -2\} \qquad (A.1)$$

$$\psi_{h,q} = 2\ln\left[\frac{(1+x^2)}{2}\right] \quad \{-0.01 > \xi > -2\} \quad (A.2)$$

where $x = (1 - 16\xi)^{1/4}$.

Stable case: Hicks (1976):

$$\psi_m = \psi_{h,q} = -5\xi, \quad \{3 \geq \xi \geq 0\}. \qquad (A.3)$$

Beljaars and Holtstag (1991):

$$-\psi_m = a\xi + b\left(\xi - \frac{c}{d}\right)\exp(-d\xi)$$

$$+ \frac{bc}{d} \quad \{7 \geq \xi \geq 3\} \tag{A.4}$$

$$-\psi_{h,q} = \left(1 + \frac{2}{3}a\xi\right)^{3/2} + b\left(\xi - \frac{c}{d}\right)\exp(-d\xi)$$

$$+ \frac{bc}{d} + 1 \quad \{7 \geq \xi \geq 3\} \tag{A.5}$$

where $a = 1$, $b = 0.667$, $c = 5$, and $d = 0.35$.

For strongly stable stratification cases, Monin–Obukhov theory has limitations. In fact, there is large scatter between theoretical fits and observed data and it is for the user to believe which one is better. Introduction of additional length scales in addition to L, namely, L_f characterizing the effect of earth's rotation and L_N characterizing the non-local effect of the static stability in the free atmosphere reduce the scatter (Zilitinkevish and Esau 2007). However, to implement these scales, additional information is required (vertical profile of the atmosphere) which is not available at places having only tower measurements.

References

Anthoni P, Law B E and Unsworth M J 1999 Carbon and water vapor exchange of an open-canopied ponderosa pine ecosystem; *Agric. For. Meteorol.* **95** 151–168.

Beljaars A C M and Holtslag A A M 1991 Flux Parameterization over Land Surfaces for Atmospheric Models; *J. Appl. Meteor.* **30** 327–341.

Bendat J S and Piersol A G 1986 *Random data analysis and measurement procedures*; 2nd edn., John Wiley & Sons.

Bhat G S, Rao P L, Sangolli V G, Bhat G P, Chandelkar A B, Rao H and Kadav V B 2005 Diurnal and intraseasonal variations observed on the west coast of India; *Mausam* **56** 97–106.

Bhat G S and Co-authors 2001 BOBMEX – the Bay of Bengal Monsoon Experiment; *Bull. Amer. Meteor. Soc.* **82** 2217–2243.

Businger J A, Wyngaard J C and Izumi Y 1971 Flux profile relationships in the atmospheric surface layer; *J. Atmos. Sci.* **28** 181–189.

Dyer A J 1974 A review of flux profile relationships; *Boundary-Layer Meteorol.* **7** 363–372.

Garratt J R 1992 *The atmospheric boundary layer*; (New York: Cambridge Univ. Press), 316 pp.

Farouki O T 1986 *Thermal properties of soil*; Series on rock and soil mechanics, Vol. 11, Trans Tech Publishers, Clausthal–Zellerfeld, Germany.

Hicks B B 1976 Wind Profile Relationships from the Wangara Experiment; *Quart. J. Roy. Meteor. Soc.* **102** 535–551.

Hollinger D Y, Goltz S M, Davidson E A, Lee J T, Tu K and Valentine H T 1999 Seasonal patterns and environmental control of carbon dioxide and water vapour exchange in an ecotonal boreal forest; *Glob. Change. Biol.* **5** 891–902.

Hosom David S, Weller R A, Payne R E and Prada K E 1995 The IMET (Improved Meteorology) Ship and buoy systems; *J. Atmos. Oceanic Technol.* **12** 527–540.

Kaimal J C and Finnigan J J 1994 *Atmospheric boundary layer flows – their structure and measurement*; (New York: Oxford University Press).

Mahrt L 2007 The influence of nonstationarity on the turbulent flux-gradient relationship for stable stratification; *Boundary-Layer Meteorol.* **125** 245–264.

Mahrt L 2008 Bulk formulation of surface fluxes extended to weak-wind stable conditions; *Quart. J. Roy. Meteor. Soc.* **134** 1–10.

Monin A S 1970 The atmospheric boundary layer; *Annu. Rev. Fluid Mech.* **2** 225–247.

Monin A S and Yaglom A M 1975 *Statistical Hydrodynamics*; MIT Press.

Nakamura R and Mahrt L 2005 A study of intermittent turbulence with CASES-99 tower measurements; *Boundary-Layer Meteorol.* **114** 367–387.

Narasimha R, Sikka D R and Prabhu A 1997 *The Monsoon Trough Boundary Layer* (Bangalore, India: Indian Academy of Sciences), 422 pp.

Panofsky H A and Dutton J A 1984 *Atmospheric Turbulence: Models and Methods for Engineering Applications.* (New York: John Wiley & Sons).

Rao Kusuma G and Narasimha R 2006 Heat flux scaling for weakly forced turbulent convection in the atmosphere; *J. Fluid. Mech.* **547** 115–135.

Rao P S 2005 Arabian Sea Monsoon Experiment: An overview; *Mausam* **56** 1–6.

Schmid H P, Grimmond C S B, Cropley F, Offerle B and Su H B 2000 Measurements of CO_2 and energy fluxes over a mixed hardwood forest in the mid-western United States; *Agric. For. Meteorol.* **103** 357–374.

Stull R B 1988 *Introduction to Boundary Layer Meteorology.* (Dordrecht, Netherlands: Kluwer Academic Publishers).

Vernekar K G, Sinha S, Sadani L K, Sivaramakrishnan S, Parasnis S S, Brij Mohan, Dharmaraj S, Patil M N, Pillai J S, Murthy B S, Debaje S B and Bagavathsingh A 2003 An Overview of the Land Surface Processes Experiment (Laspex) over a Semi-Arid Region of India; *Boundary-Layer Meteorol.* **106** 561–572.

Wilczak J M, Oncley S P and Stage S A 2001 Sonic anemometer tilt correction algorithms; *Boundary-Layer Meteorol.* **99** 127–150.

Wilson K B and Baldocchi D D 2000 Seasonal and interannual variability of energy fluxes over a broadleaved temperate deciduous forest in North America; *Agric. For. Meteorol.* **100** 1–18.

Wilson K and Co-authors 2002 Energy balance closure at FLUXNET sites; *Agric. For. Meteorol.* **113** 223–243.

Zilitinkevich S S and Esau I N 2007 Similarity theory and calculation of turbulent fluxes at the surface for the stably stratified atmospheric boundary layer; *Boundary-Layer Meteorol.* **125** 193–205.